RSC Advances

ROYAL SOCIETY OF CHEMISTRY

www.rsc.org/advances

Hierarchically structured catalyst layer for oxygen reduction reaction fabricated by electrodeposition of platinum on carbon nanotube coated carbon fiber

Raghunandan Sharma[1] and Kamal K. Kar[1, 2, *]

Advanced Nanoengineering Materials Laboratory

[1]Materials Science Programme and [2]Department of Mechanical Engineering

Indian Institute of Technology Kanpur, Kanpur-208016, India

[*]Corresponding author: Fax: +91 512 2597408; E-mail: kamalkk@iitk.ac.in (Kamal K. Kar)

Abstract

Cost-efficient fabrication of cathode catalyst layer having low Pt-loading and high oxygen reduction reaction (ORR) performance is of prime importance towards commercialization of low temperature fuel cells. Here, an attempt has been made to fabricate hierarchically structured and cathode catalyst layer consisting of Pt-nanoparticle clusters supported on defective carbon nanotube (CNT) coated carbon fiber (CNTCF). CNTs are grown on carbon fiber (CF) by chemical vapor deposition (CVD), while electrodeposition is employed to deposit Pt-nanoparticle clusters on the CNTCF. Effect of Pt-loading on oxygen reduction reaction (ORR) performance of the Pt-coated CNTCF (Pt-CNTCF) electrocatalysts is studied by varying the electrodeposition time (t_{ed}) between 5 and 30 min, which results a variation of Pt weight fraction in Pt-CNTCF from almost zero to ~0.3. Linear sweep voltammetry using the Pt-CNTCF modified glassy carbon (GC) rotating disc electrode (RDE) is employed to study the ORR performance of the samples. The CNTCF support, owing to the defective structure of CNT, itself exhibits significant ORR activity with an electron transfer number (n) of ~2.6, which leads to a synergistic enhancement of the overall electrocatalytic performance of Pt-CNTCF. For lower Pt-loading on GC (~5 μg cm^{-2}), the contribution of CNTCF support dominates, while the Pt-nanoclusters govern the ORR

performance at higher Pt-loading ((>10 μg cm^{-2}), with n>3.5. Hence, a very low Pt-loading (~5 μg cm^{-2}) may not be suitable for polymer electrolyte membrane fuel cells as production of substantial amounts of H_2O_2 on the catalyst supports may accelerate the membrane degradation.

Keywords: Platinum coated carbon nanotubes; Electrodeposition; Oxygen reduction reaction; Cluster size

1. Introduction

Heterogeneous catalysis of oxygen reduction reaction (ORR) is of utmost importance in various electrochemical devices such as low-temperature fuel cells (FCs) and metal-air batteries. Conventionally, the reaction is catalyzed by using precious metal (Pt group metals and their alloys)-based catalysts, where a typical cathode catalyst layer consists of the metallic particles supported on high surface area carbons. The requirement of large amounts of precious catalysts imposes serious limitations on the large-scale applications of these electrochemical devices.[1] Apart from the high cost, corrosion of catalyst support and the catalyst particle agglomeration impose serious durability issues on the Pt-based catalyst layers.[2] Hence, fabrication of cost-effective catalyst layers having low metal loading and high durability are of significant importance.[3-6]

Efforts towards the realization of such catalyst layers have been focused on either the reduction of Pt-loading or the Pt-free catalysts.[7, 8] To synthesize highly active catalyst layers with low-Pt loading, Pt-particles having optimized size are dispersed uniformly on a high corrosion resistant support material. Among others, carbon nanomaterials such as carbon nanotubes (CNTs) and graphene, owing to their high strength, large surface area,[9-11] high corrosion resistance[12] and excellent thermal as well as electronic conductivities,[13, 14] have been studied extensively as catalyst supports.[15-17] Their performance is affected significantly by factors such as electronic connectivity

between individual catalyst particles and catalyst support,[18] contact resistance at the catalyst layer/gas diffusion layer interface,[19] catalyst support and/or catalyst particle agglomeration,[20] catalyst layer thickness,[21] catalyst particle size,[22] etc. These factors can be controlled by employing various structural modifications in the catalyst support and/or by using different routes to deposit the catalyst particles.[23-28] Catalyst layers having various CNT arrangements such as randomly orientated, aligned or 3-dimensional (3D) networked CNTs have been studied.[18, 23, 24, 29] Among these, the 3D network formed by secondary growth of CNT on a primarily aligned CNT array has been reported to provide considerably high surface area and high internal connectivity.[29] Superior performance can also be attained by reducing the catalyst layer thickness by using high loading of Pt-nanoparticles having narrow size distribution.[25] Composites consisting of CNT coated carbon cloth/carbon paper (CC/CP) synthesized by direct growth of CNT on CC/CP have been employed as catalyst support for highly durable catalyst layers.[30-33] However, direct coating of CNT on the CC/CP covers their fibers only partially and forms a layer of CNT on the surface.

Apart from their application as catalyst support, defective carbon nanomaterials, particularly, nitrogen containing CNTs and graphene, are being studied as Pt-free electrocatalysts for ORR.[34] More recently, apart from Pt-free catalysts, N-doped CNTs/graphene have also been employed as the catalyst support for Pt-nanoparticles to fabricate catalyst layers having enhanced ORR activity compared to that of pristine CNT/graphene supported Pt.[35-37] The enhancement may be attributed to the modified structural as well as electronic configurations.[38] Chetty et al. have attributed the enhanced activity to the anchoring effect of pyridinic/pyrrolic-N sites for the metal deposition.[39] Similarly, better dispersion of Pt-nanoparticles for N-doped CNTs compared to that for CNTs has been reported.[36] More recently, Liu et al. have shown that presence of defects in the outer CNT

walls improves their ORR activity significantly.[40] However, the contribution of such defective CNT-based support on the ORR performance of the catalyst layer has not been investigated well.

Present study reports a hierarchically structured and 3D networked FC cathode/anode catalyst layer consisting of Pt-nanoparticle clusters supported on CNT coated carbon fiber (CNTCF). Here, hierarchically structured CNTCF is synthesized by direct growth of CNT on carbon fiber (CF) substrate by chemical vapor deposition (CVD). The direct growth of CNT on CF provides good electronic connectivity between CNTs and CF surface.[11, 41] The catalyst coating on CNTCF is performed by electrodeposition technique. Furthermore, effects of increasing Pt-loading on the catalytic activity are studied by varying the electrodeposition time (t_{ed}). Finally, ORR activity of Pt-coated CNT samples is compared with that of CNTCF support.

2. Experimental

2.1 Synthesis of Pt-CNTCF

The hierarchical catalyst layer was synthesized using polyacrylonitile (PAN)-based CF as the starting material, which served as the substrate to grow CNTs. CNTs as well as Pt-nanoparticles were synthesized directly on their respective substrates, namely the CF and the CNTCF. Initially, the CF was heat treated at 450 ^{o}C for 10 min to remove the polymeric sizing agent. The Ni catalyst coating on heat treated CF was performed by electroless process according to the procedure mentioned elsewhere.[41] In brief, heat treated CF was dipped for 10 min in an alkaline bath held at 80 ^{o}C, where the coating bath consisted of nickel sulphate (30 g l^{-1}), sodium hypophosphite (12 g l^{-1}), ammonium chloride (50 g l^{-1}), trisodium citrate (40 g l^{-1}) and liquor ammonia (30% NH_3 to adjust pH at 8). Before further processing, the catalyst coated CF was washed severally with deionized (DI) water and dried at ~60 ^{o}C for 2 h. Further, CNT were grown on the catalyst-coated

CF by catalytic decomposition of C_2H_2 in N_2 atmosphere using CVD. The C_2H_2 flow rate, reaction temperature and growth duration during CVD process were taken as 90 ml min^{-1}, 800 ^oC and 15 min, respectively. Further, the as-synthesized CNTCF was treated successively with 5 M HNO_3 and 0.5 M H_2SO_4 for 12 h each to remove residual Ni particles from the CNT tips.[42] Finally, to synthesize Pt coated CNTCF (Pt-CNTCF); Pt nanoparticles were deposited on the acid-treated CNTCF by electrodeposition method in a two-electrode setup using CNTCF and Pt wire as working and counter electrodes, respectively. Coating bath containing $H_2PtCl_6.6H_2O$ (1 g l^{-1}) in 0.5 M H_2SO_4 aqueous solution was used as electrolyte. Electrodeposition was performed at an applied potential of -2.0 V at t_{ed} of 5, 10, 15, 20, 25 and 30 min to synthesize samples Pt-CNT-05, Pt-CNT-10, Pt-CNT-15, Pt-CNT-20, Pt-CNT-25 and Pt-CNT-30, respectively. The parameters for electrodeposition were selected so that the Pt-loading with time varies gradually. For example, large platinum particles were obtained for electrodeposition at -3 V (Fig. S1), which possibly may not be interesting due to high Pt-loading.

2.2 Characterization of Pt-CNTCF

Scanning electron microscopy (SEM, EVO MA 15, Zeiss and field emission SEM (FESEM), JEOL JSM-7100F) was employed to study the Pt-cluster size distribution and surface morphology of Pt-CNTCF samples. Elemental analysis was performed by using energy dispersive x-ray (EDX) spectroscopy on a FEI Quanta 200 SEM. Evolution of crystalline size was studied by X-ray diffraction (XRD; Rigaku Miniflex 600 with Cu K_α (λ = 1.5418 Å) radiation) studies. Additionally, Raman spectroscopy was performed using a Horiba Jobin Yvon LabRAM HR Raman microscope equipped with a laser excitation source of 632.7 nm.

Cyclic voltammetry (CV) measurements were performed to study the catalytic performance in terms of the ORR activity and electrochemical surface area (ESA) by using a three-electrode setup

attached to an Agilent 5500 AFM. Pt-CNTCF modified glassy carbon (GC) electrode (φ = 3 mm) was used as the working electrode, while Ag/AgCl (1 M KCl) and Pt-wire electrodes served as reference and counter electrodes, respectively. To prepare a working electrode, 10 mg of Pt-CNTCF was dispersed in 2 ml C_2H_5OH by ultrasonication for 1 h and 5 µl of the dispersion was drop-casted on a cleaned GC electrode and dried for 1 h. Electrocatalytic activity towards ORR was measured by CV in O_2 saturated 0.1 M KOH for a potential scan ranging from -1.0 to 0.2 V at a scan rate of 50 mV s^{-1}. Similarly, ESA was calculated by hydrogen desorption peak from the CV curve in 1.0 M H_2SO_4 for a potential scan between -0.1 to 0.8 V at a scan rate of 50 mV s^{-1}. Similarly, linear sweep voltammetry (LSV) was performed on a homemade rotation disk electrode (RDE) setup.[43, 44] The amount of Pt loaded on the Pt-CNTCF modified working electrode was estimated by thermogravimetric analysis (TGA) using a Perkin-Elmer Diamond TG/DTA analyzer. TGA of the Pt-CNTCF dispersion (250 µl) used to prepare modified GC electrode was performed in O_2 environment (flow rate: 200 ml min^{-1}) from 40 to 750 ^oC at a heating rate of 10 ^oC min^{-1}.

3. Results and discussion

3.1 Structural hierarchy of Pt-CNTCF

As shown in Fig. 1, the multiscale hierarchical structure of the catalyst layer consists of a mat of CNTCF over which, Pt-nanoparticles were electrodeposited to form Pt coated CNTCF (Pt-CNTCF). The structure possesses a three-level hierarchy at various length scales. At microscale, a single CF strand consists of thousands of microsized fibers. Similarly, at submicroscale, each fiber is coated by Pt-coated CNTs while at nanoscale; Pt-nanoparticle clusters are coated on CNTs. The unique structure may provide improved interactions between CNT–CF as well as CNT–Pt

interfaces, and hence better electronic connectivity of the catalyst particles within the catalyst layer. Thus, the electron transport from/to catalyst particle can find an easy path through the microsized CF.

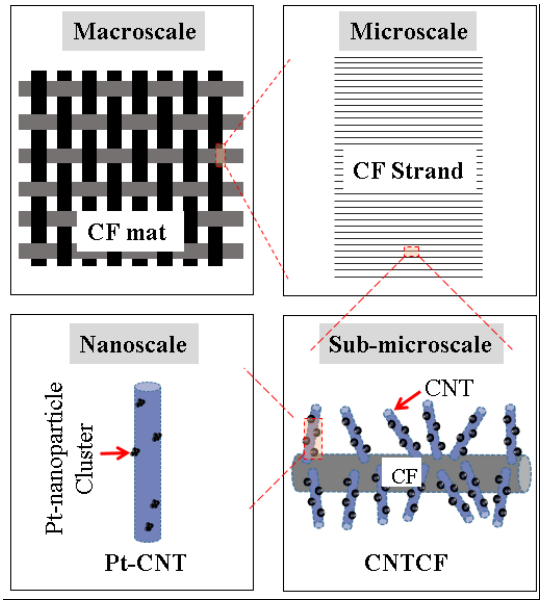

Fig. 1: Schematic of hierarchically structured catalyst layer consisting of Pt-CNTCF at different length scales.

3.2. Structural characterizations

Fig. 2a shows the SEM image of electroless Ni-coated CF revealing the deposition of Ni in form of particulate clusters having diameter of ~120 nm. XRD pattern of the Ni coated CF shown in Fig. 2b exhibits the diffraction peaks at ~26, ~45 and 52°, which correspond to graphitic C(002) (JCPDS 41-1487), Ni(111) and Ni(200) (JCPDS- 87-0712), respectively. Elemental analysis of the catalyst deposits by EDX (Fig. 2c) shows the presence of Ni (~15 at.%) and P (~1 at.%), suggesting the presence of nickel phosphides (NiP, NiP_2, etc.) in small fractions along with Ni. SEM image of as-synthesized CNTCF (Fig. 2d) shows dense CNT coating on the CF surface with no uncovered CF surface being observable. Ni particles are visible as bright spots on the CNT tips

Fig. 2d, inset), which are removed during acid-treatment. Hence, the acid-treated CNTCF consists of CF surface covered by catalyst-free CNTs of diameters ranging between ~150 to 200 nm (Fig. 2e). The surface of acid-treated CNT exhibits rough structure due to the presence of groove-like structures that are formed possibly due to the partial corrosion of the outer CNT walls during acid-treatment. The removal of acid-unstable part of CNT before Pt coating is favorable towards high durability of the catalyst support. Moreover, the rough corroded surface may also provide active sites for Pt electrodeposition. Raman spectra of as-synthesized and acid-treated CNTs (Fig. 2f) exhibit their graphitic nature with presence of intense D-band, attributable to highly defective nature of the CNTs. Again, the Raman D-band to G-band intensity ratio (I_D/I_G) decreases from 1.53 for as-synthesized CNTs to 1.17 for acid-treated CNTs, which is contrary to the fact that the number of defects in CNTs increases with acid-treatment.[45] This may be attributed to the decreased number of defects due to the removal of highly defective/amorphous carbon during acid-treatment, which dominates the concurrent increase due to degradation of outer CNT walls.

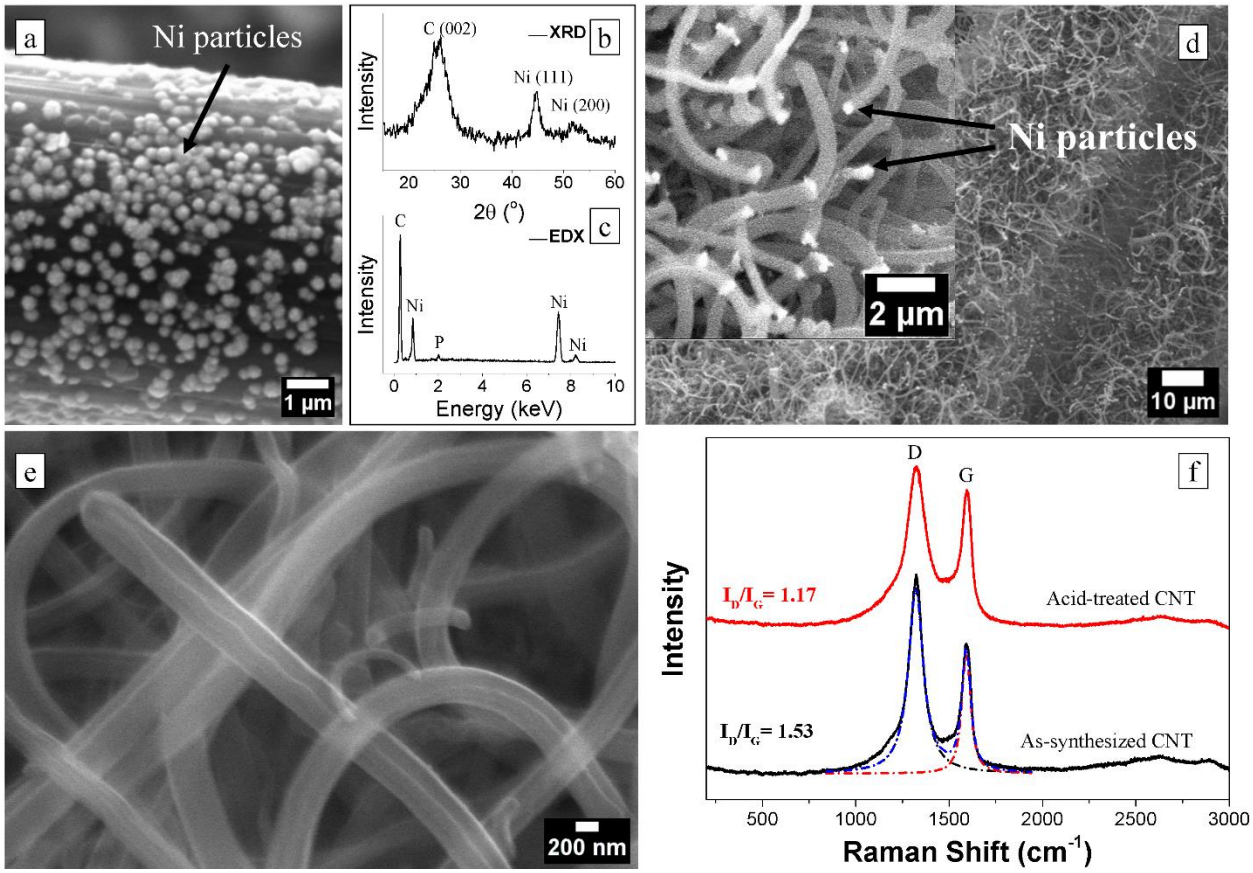

Fig. 2: (a) SEM image (b) XRD pattern and (c) EDX spectrum of catalyst-coated CF. (d) SEM image of CNTCF showing dense CNT forest grown on CF. Inset of (d) shows Ni nanoparticles on the CNT tips. (d) Higher magnification SEM image of acid-treated CNTCF. Inset of (e) shows the TEM image of (e). (f) Raman spectra of as-synthesized and acid-treated CNT. Typical Voigt fits to Raman D- and G-bands of the as-synthesized CNTs are shown by dotted curves.

3.3. Pt electrodeposition on CNTCF

SEM and FESEM and TEM images of Pt-CNTCF are shown in Fig. 3. Individual CFs are covered with a thick (~10 μm) CNT forest, while Pt-nanoparticle clusters (~100 nm) are coated uniformly on the CNTs. Higher magnification FESEM image of Pt coated CNT shown as the inset of Fig. 3b reveal individual Pt-nanoparticles of ~10 nm average diameters in the cluster. Deposition of such

Pt-clusters on CNT is possibly due to the presence of large diameter (~100 nm; of the order of CNT diameter) active sites on CNT surface formed during acid-treatment, where the nucleation of multiple particles takes place. The presence of Pt is confirmed by EDX analysis, which reveals increasing weight fraction of Pt from ~0 to ~0.3 with increasing t_{ed} from 5 to 30 min (Supplementary information; Fig. S2).

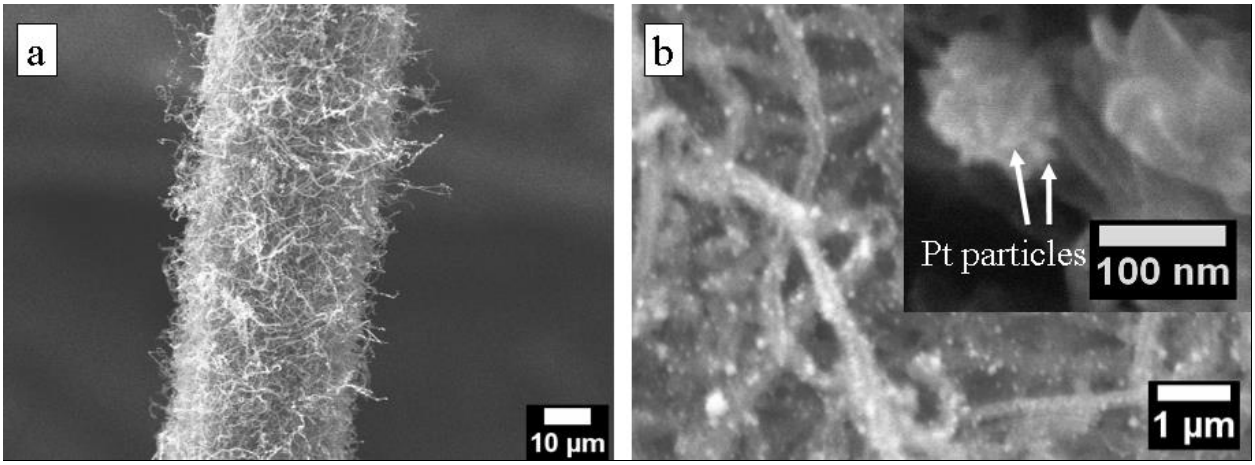

Fig. 3: SEM images of Pt-CNTCF for t_{ed} of 20 min revealing (a) Single CF covered with thick forest of Pt-coated CNT and (b) a coating of Pt-nanoparticle clusters on CNT. Inset of (b) shows the FESEM image of a Pt cluster revealing individual Pt-nanoparticles.

Pt-cluster size distributions of Pt-CNTCF for varying t_{ed} are shown in (Supplementary information; Fig. S3). To obtain the Pt-cluster size distribution of a typical Pt-CNTCF sample, areas of individual Pt-clusters visible in the SEM image were approximated by the areas of ellipses encircling them. Significant increments in the cluster density (number of cluster/area) are observed with increasing t_{ed}, suggesting continuous formation of new clusters as well as the growth of individual particles of a cluster during the electrodeposition process.

Fig. 4a shows the thermal drift corrected TGA of the Pt-CNTCF dispersion (250 µl), performed in O_2 atmosphere at a heating rate of 10 $^oC\ min^{-1}$. A correction for thermal drift is performed by TGA

of an empty sample pan under similar conditions and the weight drift during heating was recorded. The final thermal drift calculated by fitting the data with a polynomial of order three is used to correct the TGA data (inset; Fig. 4a). Residual weight of the drift corrected TGA plots, which exhibits an increasing trend with t_{ed}, is considered as the net weight of Pt-nanoparticles in 250 µl dispersion. The variations of Pt-cluster size (D_{Pt}), % area coverage and the Pt loading on GC/electrode area (w_{Pt}), with t_{ed} have been shown in Fig. 4b. With increasing t_{ed} from 10 to 30 min, D_{Pt} exhibits large increments from ~70 to ~170 nm. However, for t_{ed} below 20 min, D_{Pt} increases marginally owing to the combined effects of the growth of existing clusters and the formation of new ones. Again, with increasing t_{ed} from 05 to 30 min, the Pt-loading increases from 3.8 to 15.7 µg cm^{-2}, while the fractional area coverage changes from ~0.5 to ~15 %. For higher t_{ed}, the area coverage reaches towards saturation due to overlapping of individual clusters.

The variation of Pt-loading and area coverage with t_{ed} exhibit a complex behavior revealing the rate of deposition being highest between t_{ed} of 10 to 15 min, followed by saturation. This may be attributed to the combined effects of the nucleation and growth of Pt-nanoparticles and the decreasing Pt-ion concentration in the coating bath with increasing t_{ed}. Initially, the rate of deposition remains low during the incubation period, while it increases with t_{ed} due to particle growth until the Pt-ion concentration depletes. Similarly, for t_{ed} below 20 min, D_{Pt} increases marginally owing to the combined effects of the growth of existing clusters and the formation of new ones. For higher t_{ed}, the D_{Pt} exhibits fast growth due to overlapping of individual clusters.

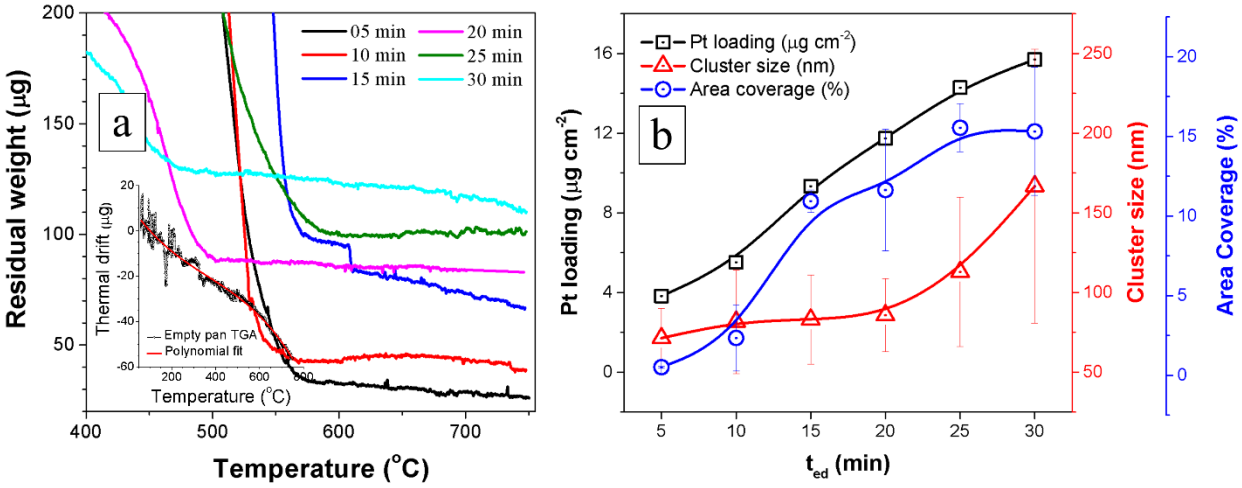

Fig. 4: (a) TGA of Pt-CNTCF dispersion (250 µl) corrected for thermal drift by using empty pan TGA data shown in the inset. (b) Variations of average Pt-cluster size, % area coverage and Pt loading on GC/electrode area (w_{Pt}), with the deposition time t_{ed}.

Typical XRD pattern of Pt-CNTCF for t_{ed} of 30 min is shown in Fig. 5. Presence of diffraction peak at 2θ of ~26° corresponding to (002) plane of graphite (JCPDS 41-1487) reveals the graphitic structure of CNTCF substrate. Again, the presence of diffraction peaks at 2θ of ~40, ~47, ~68 and ~81° corresponding respectively to Pt(111), Pt(200), Pt(220) and Pt(311) planes (JCPDS 87-0642) reveal the coating of polycrystalline Pt-nanoparticles. XRD patterns of the inset of Fig. 5 show the variation of Pt(111) and Pt(200) peaks with t_{ed}. With increasing t_{ed}, the intensity of individual diffraction peak increases due to the larger number of the Pt-crystallites. However, area ratios of Pt(111) and Pt(200) peaks exhibit no significant variation, revealing similar crystallographic orientation for all the Pt-CNTCF samples. Similarly, the Pt-crystalline size also remains constant at ~10 nm, which suggests a continuous nucleation of Pt-particles during electrodeposition.

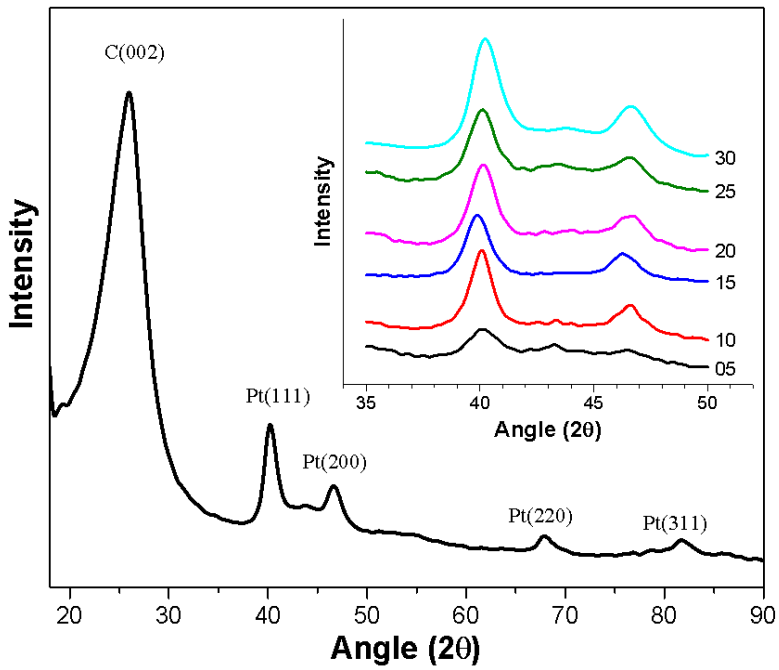

Fig. 5: XRD pattern of Pt-CNTCF for t_{ed} of 30 min. Inset shows the variation of Pt(111) and Pt(200) peaks with t_{ed} from 5 to 30 min.

3.4. Electrocatalytic activity of Pt-CNTCF

Electrocatalytic performance of Pt-CNTCF synthesized at varying t_{ed} is studied in terms of the specific electrochemical surface area (ESA) and ORR activity in alkaline media. Both hydrogen underpotential deposition (H upd) and copper upd (Cu upd) were performed to study the ESA variation. However, as the Cu stripping peak of Pt-coincides with that of the CNTCF support (Fig. S4), the ESA was calculated by using H upd using CV in Ar saturated 1.0 M H_2SO_4 at a scan rate of 50 mV s^{-1}. Fig. 6a exhibits the evolution of hydrogen desorption (H_{des}) peak of Pt-CNTCF modified GC electrodes with t_{ed}. Since the integrated area of H_{des} peak corresponds to the total charge associated with H^+ desorption (Q_H), assuming adsorption of H^+ monolayer on Pt with one to one H-Pt correspondence, the ESA is given by $ESA\ [cm^2/g] = Q_H[\mu C]/(210 \times w_{Pt}[g])$,[46] where 210 μC/$cm^2$ is the charge/cm^2 of hydrogen monolayer adsorbed on polycrystalline Pt,[47]

while w_{Pt} is the Pt-loading on electrode, determined by TGA data. Again, Q_H is calculated from the H_{des} peak of the CV curve using the relation– $Q_H = (1/scan\ rate) \int idV$, where $\int idV$ being the area of the hydrogen desorption peak assumed to be in between 0.05 to -0.1 V (vs. Ag/AgCl). Variation of ESA with t_{ed} is shown in Fig. 6b. Low ESA for t_{ed} of 5 min may be attributed to the lower Pt-loading, at which large fraction of the Pt-nanoparticles may remain obscured by the CNTs, when the CNT dispersion is drop-casted on the electrode. Again, ESA increases monotonously for t_{ed} of 10-25 min due to increased number of Pt-nanoparticle clusters, while decreases slightly for higher t_{ed} owing to overlapping of the clusters to reduce the effective surface area. The maximum value of the ESA is observed to be ~82 $m^2\ g^{-1}$ for t_{ed} of 25 min.

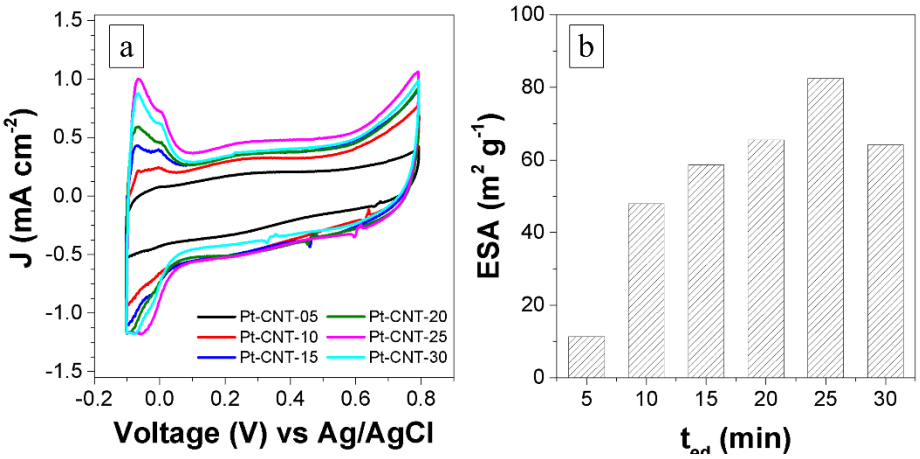

Fig. 6: (a) CV scans of Pt-CNTCF in Ar saturated 1.0 M H_2SO_4 at a scan rate of 50 mV s^{-1}. (b) Variation of ESA with t_{ed}.

The ORR activity of Pt-CNTCF was studied in alkaline media through the CV (stationary electrodes) and the LSV (RDE; 1600 rpm) measurements in O_2 saturated 0.1 M KOH electrolytes using Pt-CNTCF modified GC working electrodes. CV scans of Pt-CNTCF electrodes in O_2 saturated electrolyte at a potential scan rate of 50 mV s^{-1} are shown in Fig. 7, where a cathodic peak at ~-0.4 V (vs. Ag/AgCl), is observed. The cathodic peak, which disappears in Ar saturated

electrolyte (Supplementary information; Fig. S5), corresponds to the ORR. The variation of ORR performance of Pt-CNTCF with varying t_{ed} can be analyzed qualitatively in terms of the intensity of ORR peak. As can be inferred from Fig. 7, ORR peak intensities remain high for t_{ed} between 10 to 20 min, which can be attributed to the increasing number and the uniform dispersion of agglomeration-free Pt-nanoparticles. With further increase in t_{ed} beyond 20 min, despite increasing wt.$_{Pt}$, current reduces due to the reduction in the effective surface area by overlapping Pt-clusters.

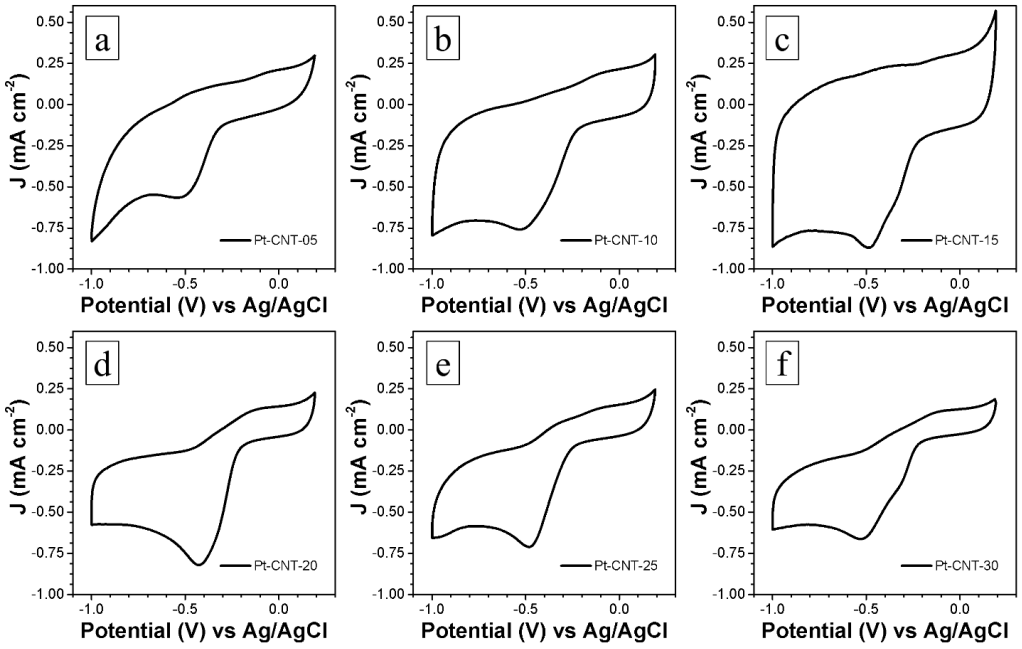

Fig. 7: CV scans of Pt-CNTCF in O_2 saturated 0.1 M KOH at a scan rate of 50 mV s^{-1}

Variation of ORR activity with t_{ed} was further studied by LSV using Pt-CNTCF modified GC working RDE (1600 rpm) in 0.1 M KOH at a potential scan rate of 10 mV s^{-1} (Fig. 8a). The corresponding Tafel plots are shown in Fig. 8b. As defective CNTs are known to show catalytic activity for ORR,[40] LSV corresponding to CNTCF (without Pt coating) has also been incorporated. The CNTCF modified GC electrode was prepared through a route similar to that adopted to prepare

the Pt-CNTCF modified GC. As can be seen from Fig. 8a, the CNTCF modified GC electrode exhibits significant ORR current and hence contributes to the overall ORR activity, owing to the defective structure of CNTs (Fig. 2f; Raman spectroscopy). The variation of ORR activity of Pt-CNTCF with t_{ed} is evaluated in terms of ORR onset potential (V_{Onset}), ORR current ($|J_{ORR}|$), and Tafel slope, with higher ORR activity being characterized by high $|J_{ORR}|$, more positive value of V_{Onset}, and lower Tafel slope.[43, 48] The parameter V_{Onset} is estimated from the intersection point of the tangents to the LSV curve in the proximity of ORR peak, while $|J_{ORR}|$ is taken as the current density at a potential of -0.3 V. Variation of $|J_{ORR}|$ shown in Fig. 8c suggests low ORR activity for t_{ed} of 5 min, which increases with increasing t_{ed} to reach a saturation for t_{ed} above 15 min. For example, $|J_{ORR}|$ exhibits a two-fold increment with increasing t_{ed} from 5 to 15 min. Again, variations of the V_{Onset} and Tafel slope with t_{ed} shown in Fig. 8d exhibit similar trends with respective shifts from ~-190 to ~-75 mV and from 190 to 120 mV/decade with increasing t_{ed} from 5 to 20 min. Compared to Pt-CNTCF, CNTCF exhibits a more negative V_{Onset} of ~-200 mV and a larger Tafel slope of ~240 mV/decade. The large variation of V_{Onset} and Tafel slope with t_{ed} may be attributed to the varying relative contributions of the CNT support and the supported Pt-nanoparticles to the overall ORR current, where the ORR current from CNT support dominates at lower t_{ed}. Variations of the parameters V_{Onset} and Tafel slope suggest different nature of ORR active sites and hence, different ORR mechanisms for the CNT support and the supported Pt.

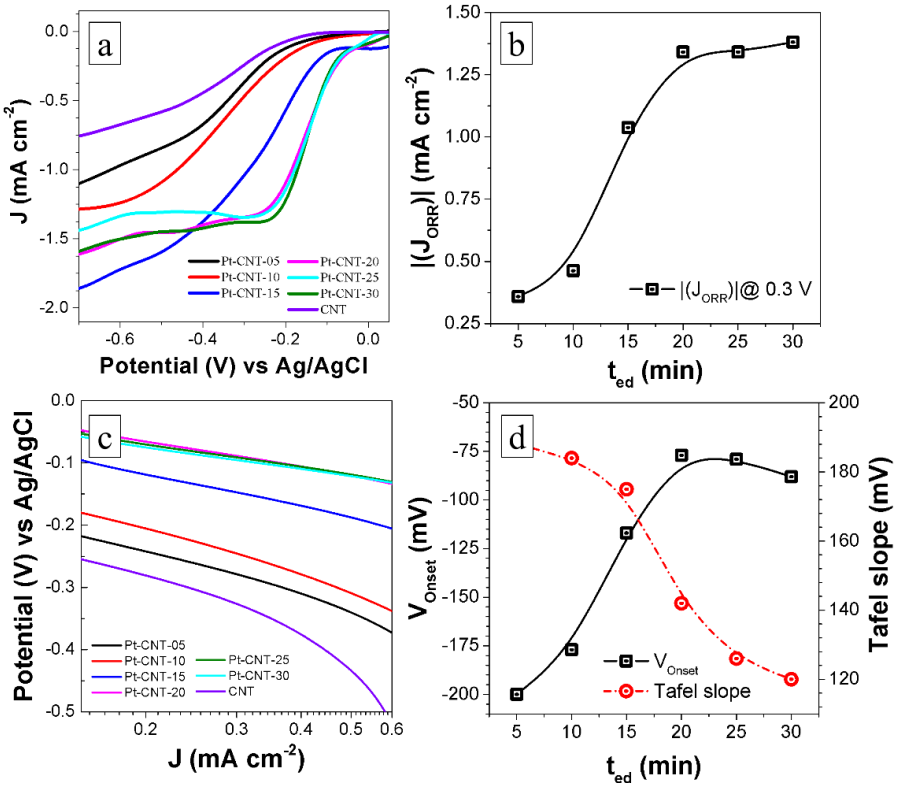

Fig. 8: (a) LSV curves of Pt-CNTCF modified GC RDE (1600 rpm) in O_2 saturated 0.1 KOH at a potential scan rate of 10 mV s^{-1}. (b) Tafel plots obtained from (a) with solid lines showing linear fits to data. (c) Variation of ORR current at -0.3 V ($|J_{ORR}|$) with t_{ed}. (d) Variations of ORR onset potential (V_{Onset}) and Tafel slope.

LSV curves at different rotation rates were obtained for Pt-disk (2 mm diameter), Pt-CNTCF modified and CNT modified GC RDEs (Fig. 9a-c). Further, to understand the nature of ORR active sites, the measured disk current density (j_d) is applied to Koutecky - Levich (KL) equation (eq. 1).[49]

$$\frac{1}{j_d} = \frac{1}{j_k} + \frac{1}{j_{diff}} = \frac{1}{j_k} + \frac{1}{B\omega^{0.5}}, \quad (1)$$

where j_k and j_{diff} are the kinetic and diffusion-limiting current densities, ω is the angular velocity of RDE and B is a constant dependent on concentration and diffusion coefficient of O_2, kinematic viscosity of the electrolyte and electron transfer number (n) through eq. 2.

$$B = 0.62nFC_0D_0^{2/3}v^{-1/6} = nA, \text{ with } A = 0.62FC_0D_0^{2/3}v^{-1/6} \quad (2)$$

For the present RDE setup, the value of A is obtained from the averaged slope of the KL plots (j_d^{-1} vs. $\omega^{-0.5}$; Fig. 9d) at -0.45 and -0.50 V for Pt RDE by assuming n=4 for Pt. Again, n values for Pt-CNTCF (t_{ed}=20 min) as well as CNT modified GC RDEs are obtained from the slopes of corresponding KL plots (Fig. 9e, f). Values of n for bare CNT and Pt-CNTCF are calculated to be 2.57 and 3.53, respectively. This suggests the dominance of two-electron pathway of ORR on CNT support, which reduces the overall n value for Pt-CNTCF.

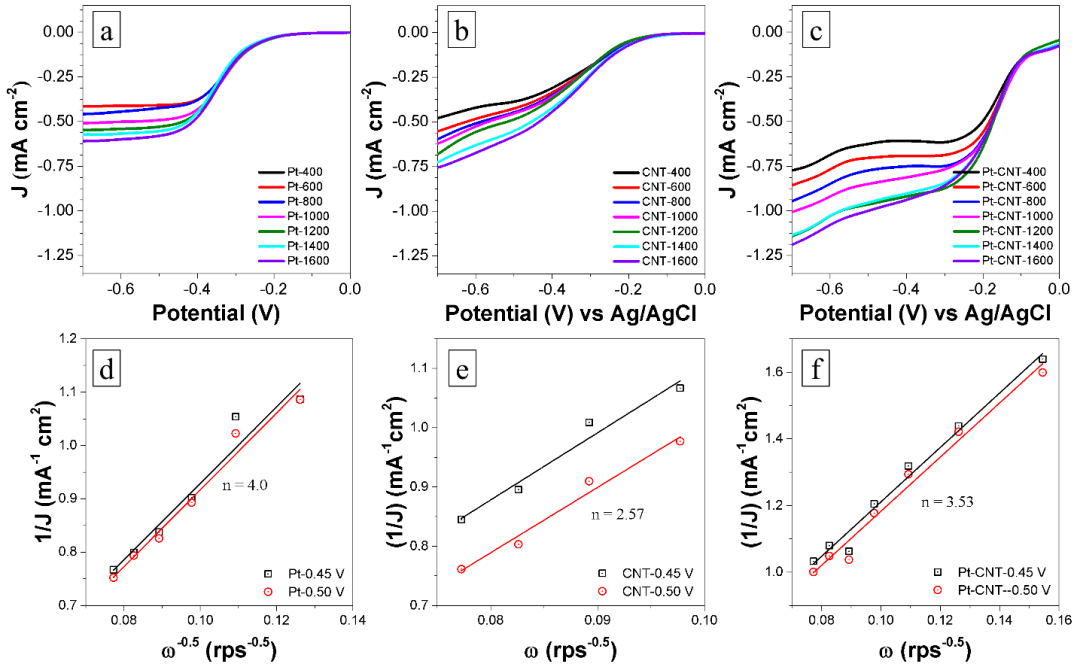

Fig. 9: (a-c) RDE voltammograms at varying rotation rates and KL plots for (a) Pt-disk RDE, and (b) CNT support and (c) Pt-CNTCF modified GC RDEs. (d-e) KL plots corresponding (d) Pt-disk, (e) CNT support and (f) Pt-CNTCF.

Since the electrodeposition process depends not only on t_{ed} but also on other parameters such as temperature, applied potential, electrolyte composition and concentration, etc., wt.$_{Pt}$ has been considered as the key parameter affecting the electrocatalytic activity of Pt-CNTCF, instead of t_{ed}.

Fig. 10 depicts the variations of the electrochemical activity of Pt-CNTCF in terms of the parameters$|J_{ORR}|$, V_{Onset} and Tafel slope with respect to Pt-loading and Pt-cluster size (D_{Pt}). With increasing Pt-loading from ~0.2 to 0.6 μg, ORR activity of the Pt-CNTCF increases monotonously while remains practically constant for higher Pt-loading (0.6 –1.2 μg). Similarly, variations of the electrochemical activity in terms$|J_{ORR}|$, V_{Onset} and Tafel slope with D_{Pt} are exhibited in Fig. 10c, d. With increasing D_{Pt} beyond 100 nm, the ORR parameters exhibit constant values with no significant dependence on D_{Pt}. This is attributed to the reduction of the ESA with the increase in Pt-loading. The saturation of ORR activity of Pt-CNTCF for higher loading of Pt is contrary to the known behavior of Pt-based ORR electrocatalysts having lower overpotential for higher Pt-loading.[50] This can be understood by the fact that ESA reduces from 82 to 64 $m^2 g^{-1}$ with increasing Pt-loading from ~14 to ~16 μg cm^{-2} due to increased overlapping of Pt-clusters. Hence, Pt-CNTCF having a high Pt-loading with agglomeration-free Pt-clusters can provide the highest ORR performance. Moreover, as the Pt-ion concentration of the coating bath decreases with time during electrodeposition, growth of Pt-nanoparticles having different surface crystallographic orientations (*hkl*) could be possible. Such preferred orientation may affect the ORR performance significantly.[51] However, the possibility is discarded as XRD analysis reveals no such preferred orientation, confirming the variation of ORR performance to be attributed solely to the varying Pt-loading and the extent of Pt-cluster overlapping.

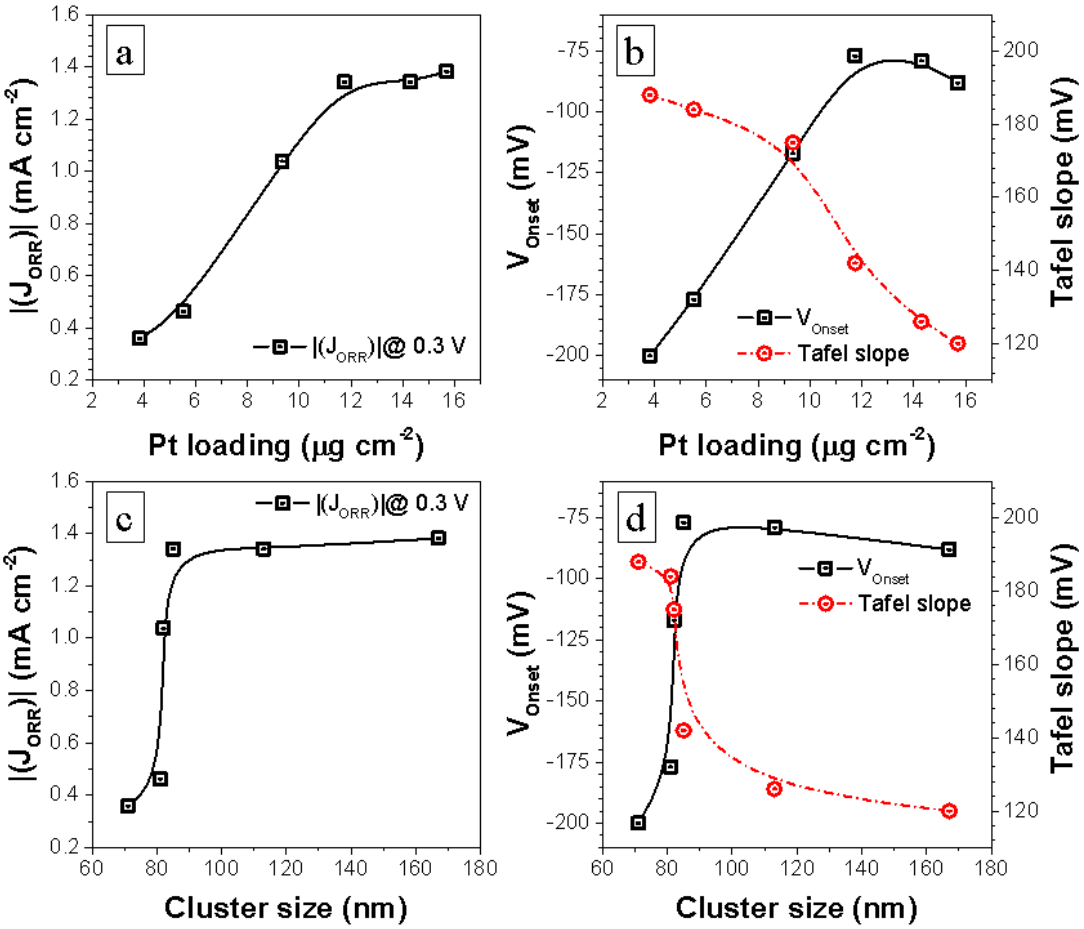

Fig. 10: (a, b) Variations of the parameters (a)$|J_{ORR}|$ and (b) V_{Onset}, Tafel slope with Pt-loading/area on the Pt-CNTCF modified GC electrode. (c, d) Correlations between cluster size and ORR parameters (a) $|J_{ORR}|$ at -0.3 V and (b) V_{Onset}, Tafel slope.

Finally, electrochemical stability of Pt-CNTCF modified GC (t_{ed} = 60 min) is investigated by potential cycling between -1.0 to 0.2 V in air saturated 0.1 M KOH electrolyte at a scan rate of 50 mV s^{-1} and the area under hydrogen desorption peak (forward scan) between -0.80 to 0.55 V is measured. Comparatively higher Pt loading (t_{ed} = 60 min) is used for the stability study to obtain a measurable peak area. For initial 100 cycles, the area shows a small (<2%) decrease. The Pt-CNTCF electrocatalysts exhibit high stability as the peak area shows a reduction of < 2% in first 100 potential cycles (Fig. 11). Hence, the Pt-nanoparticles supported on defective CNTs may be

used to fabricate cathode catalyst layers having high stability, low Pt-loading and high ORR activity.

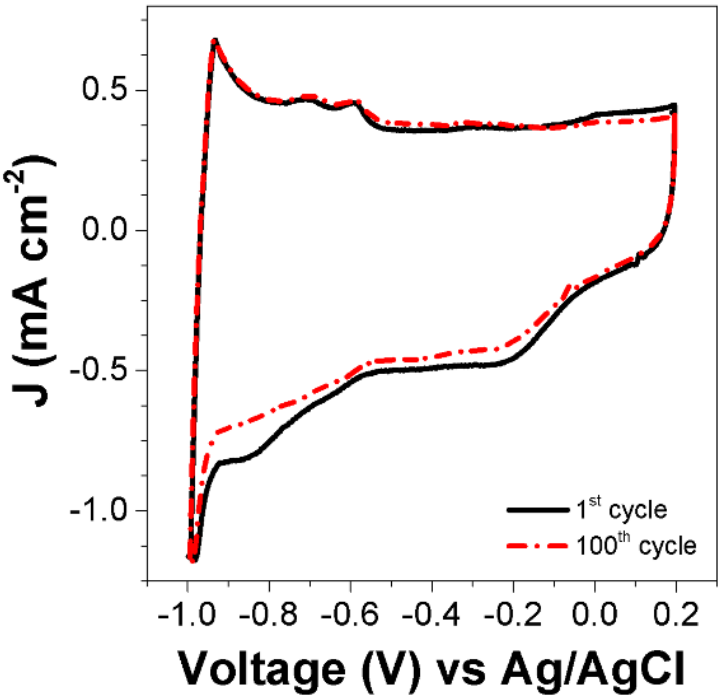

Fig. 11: Electrochemical stability of Pt-CNTCF (t_{ed} = 60 min) modified GC electrode in air saturated 0.1 M KOH at a scan rate of 50 mV s^{-1}.

The hierarchically structured CNTCF supported Pt-based catalyst layer exhibits high ORR performance in terms of both ORR and ESA. Table 1 compares the ESA and ORR performance of the present catalysts with those of a few previously reported ones. The ORR performance of various catalysts has been compared in terms of ORR current (I_{ORR}; A g_{Pt}^{-1}) at -0.3 V obtained from RDE measurements under similar conditions (0.1 M KOH, Ag/AgCl reference). The present catalysts exhibit superior ORR performance (> 2×) in terms of both the ESA as well as the I_{ORR}. Hence, catalyst layers with high ORR performance and low-Pt-loading can be fabricated by using the defective CNT coated CF as the catalyst support.

Table 1: Comparison of I_{ORR} and ESA with literature

Parameter	Literature value	Present work
I_{ORR} at -0.3 V ($A\ g_{Pt}^{-1}$)*	[52]Pt/C: 47	90 – 115
ESA ($m^2\ g^{-1}$)	[30]Pt/CNT/CP: 52	70 – 80
ESA ($m^2\ g^{-1}$)	[37]Pt/CNx: 55.6; Pt/CNT: 40.9	
ESA ($m^2\ g^{-1}$)	[53]Pt/Pt-Ni alloy: 33-62	
ESA ($m^2\ g^{-1}$)	[54]Pt_xIr_y/MWCNT: 48-98	
ESA ($m^2\ g^{-1}$)	[55]Functionalized Pt/CNT: 71	
ESA ($m^2\ g^{-1}$)	[56]Pt/SWCNT/CNF: ~ 39 – 43	
*I_{ORR} = Current density at -0.3 V from RDE plots ($A\ cm^{-2}$)/Pt loading on the RDE ($g_{Pt}\ cm^{-2}$)		

However, the low electron transfer number (n=2.57) of ORR active CNT support suggests production of H_2O_2 during ORR. As H_2O_2 is known to cause damage to the perfluorosulfonated electrolyte membranes,[57] use of such defective carbon supported, low Pt-loading catalyst layers in PMEFCs may decrease their durability. Again, as facile synthesis of defect-free CNTs is difficult, production of small amounts of H_2O_2 during operation of the fuel cells based on carbon supported cathode catalyst layers is inevitable. Hence, at low Pt-loadings, where the ORR current from catalyst support is substantial, the defective nature of CNTs and other carbonous catalyst supports may not be suitable, particularly for PEMFCs.

Conclusions

In conclusion, hierarchically structured catalyst layers are synthesized by using CNTCF as the substrate, on which Pt-nanoparticle clusters are deposited by electrodeposition process. Clusters of Pt-nanoparticles having an average particle diameter of ~10 nm and varying cluster size (~80 – ~170 nm) are grown on CNTCF by varying the deposition time. The formation of clusters is attributed to the nucleation of Pt nanoparticles only at preferred active sites on the CNT surface. With increasing deposition time, although the Pt-loading on CNTCF increases nearly linearly, the

ORR performance of Pt-CNTCF attains a saturation after initial increase, due to overlapping of Pt-clusters at higher Pt-loading. Furthermore, the CNTs used for Pt-nanoparticle support also exhibit significant ORR activity owing to their defective nature. Overall ORR activity of Pt-CNTCF is enhanced synergistically due to presence of Pt-nanoparticle clusters on defective CNT surface. The synthesized hierarchical Pt-CNTCF can be used to fabricate PEMFC/AFC catalyst layers having high performance and low Pt-loading. However, reduction of Pt-loading beyond certain limit may reduce the durability of polymer electrolytes due to production of substantial amounts of H_2O_2 on ORR active CNT supports (n=2.57).

Acknowledgements

This work was financially supported by the Department of Science and Technology, Government of India, Mission on Nano Science and Technology (Nano Mission).

References

1. S. Litster and G. McLean, *J. Power Sources*, 2004, **130**, 61-76.
2. Y. Shao, G. Yin and Y. Gao, *J. Power Sources*, 2007, **171**, 558-566.
3. K. Gong, F. Du, Z. Xia, M. Durstock and L. Dai, *Science*, 2009, **323**, 760-764.
4. S. Pylypenko, S. Mukherjee, T. S. Olson and P. Atanassov, *Electrochim. Acta*, 2008, **53**, 7875-7883.
5. H. Meng and P. K. Shen, *Electrochem. Commun.*, 2006, **8**, 588-594.
6. B. Li and S. H. Chan, *Int. J. Hydrogen Energy*, 2013, **38**, 3338-3345.
7. Z. Qi and A. Kaufman, *J. Power Sources*, 2003, **113**, 37-43.
8. A. Morozan, B. Jousselme and S. Palacin, *Energy Environ. Sci.*, 2011, **4**, 1238-1254.

9. R. R. Bacsa, C. Laurent, A. Peigney, W. S. Bacsa, T. Vaugien and A. Rousset, *Chem. Phys. Lett.*, 2000, **323**, 566-571.

10. E. A. d. Morais, G. Alvial, R. Longuinhos, J. M. A. Figueiredo, R. G. Lacerda, A. S. Ferlauto and L. O. Ladeira, *Mater. Res.*, 2011, **14**, 403-407.

11. J. Cherusseri and K. K. Kar, *RSC Advances*, 2015, **5**, 34335-34341.

12. Y. Shao, G. Yin, J. Zhang and Y. Gao, *Electrochim. Acta*, 2006, **51**, 5853-5857.

13. T. W. Ebbesen, H. J. Lezec, H. Hiura, J. W. Bennett, H. F. Ghaemi and T. Thio, *Nature*, 1996, **382**, 54-56.

14. E. Pop, D. Mann, Q. Wang, K. Goodson and H. Dai, *Nano Lett.*, 2005, **6**, 96-100.

15. C. Hu, Y. Guo, Y. Cao, L. Yang, Z. Bai, K. Wang, P. Xu and J. Zhou, *Mater. Sci. Eng., B*, 2011, **176**, 1467-1473.

16. M. Sahoo, B. P. Vinayan and S. Ramaprabhu, *RSC Advances*, 2014, **4**, 26140-26148.

17. W. Yuan, S. Lu, Y. Xiang and S. P. Jiang, *RSC Advances*, 2014, **4**, 46265-46284.

18. W. Zhang, P. Sherrell, A. I. Minett, J. M. Razal and J. Chen, *Energy Environ. Sci.*, 2010, **3**, 1286-1293.

19. I. Nitta, O. Himanen and M. Mikkola, *Electrochem. Commun.*, 2008, **10**, 47-51.

20. F. Maillard, S. Schreier, M. Hanzlik, E. R. Savinova, S. Weinkauf and U. Stimming, *Phys. Chem. Chem. Phys.*, 2005, **7**, 385-393.

21. S. Kamarajugadda and S. Mazumder, *J. Power Sources*, 2008, **183**, 629-642.

22. H. Yano, J. Inukai, H. Uchida, M. Watanabe, P. K. Babu, T. Kobayashi, J. H. Chung, E. Oldfield and A. Wieckowski, *Phys. Chem. Chem. Phys.*, 2006, **8**, 4932-4939.

23. Z. He, J. Chen, D. Liu, H. Tang, W. Deng and Y. Kuang, *Mater. Chem. Phys.*, 2004, **85**, 396-401.

24. H. Tang, J. Chen, S. Yao, L. Nie, Y. Kuang, Z. Huang, D. Wang and Z. Ren, *Mater. Chem. Phys.*, 2005, **92**, 548-553.

25. S. Li, H. Liu, Y. Wang, W. Xu, J. Li, Y. Liu, X. Guo and Y. Song, *RSC Advances*, 2015, **5**, 8787-8792.

26. L. Jiang, A. Hsu, D. Chu and R. Chen, *J. Electrochem. Soc.*, 2009, **156**, B643-B649.

27. G. Z. Hu, F. Nitze, X. Jia, T. Sharifi, H. R. Barzegar, E. Gracia-Espino and T. Wagberg, *RSC Advances*, 2014, **4**, 676-682.

28. K. Yoshii, T. Tsuda, T. Arimura, A. Imanishi, T. Torimoto and S. Kuwabata, *RSC Advances*, 2012, **2**, 8262-8264.

29. W. Xiong, F. Du, Y. Liu, A. Perez, M. Supp, T. S. Ramakrishnan, L. Dai and L. Jiang, *J. Am. Chem. Soc.*, 2010, **132**, 15839-15841.

30. S. Takenaka, H. Matsumori, H. Matsune, E. Tanabe and M. Kishida, *J. Electrochem. Soc.*, 2008, **155**, B929-B936.

31. C. H. Wang, H. Y. Du, Y. T. Tsai, C. P. Chen, C. J. Huang, L. C. Chen, K. H. Chen and H. C. Shih, *J. Power Sources*, 2007, **171**, 55-62.

32. C.-T. Hsieh, W.-M. Hung and W.-Y. Chen, *Int. J. Hydrogen Energy*, 2010, **35**, 8425-8432.

33. P. H. Maheshwari and R. B. Mathur, *Electrochim. Acta*, 2009, **54**, 7476-7482.

34. K. K. Kar, S. Rana and J. K. Pandey, *Handbook of polymer nanocomposites. Processing, performance and application*, Springer, Berlin Heidelberg, 2015.

35. D. C. Higgins, F. M. Hassan, M. H. Seo, J. Y. Choi, M. A. Hoque, D. U. Lee and Z. Chen, *J. Mater. Chem. A*, 2015, **3**, 6340-6350.

36. Y. Chen, J. Wang, H. Liu, M. N. Banis, R. Li, X. Sun, T.-K. Sham, S. Ye and S. Knights, *J. Phys. Chem. C*, 2011, **115**, 3769-3776.

37. M. S. Saha, R. Li, X. Sun and S. Ye, *Electrochem. Commun.*, 2009, **11**, 438-441.

38. D. C. Higgins, D. Meza and Z. Chen, *J. Phys. Chem. C*, 2010, **114**, 21982-21988.

39. R. Chetty, S. Kundu, W. Xia, M. Bron, W. Schuhmann, V. Chirila, W. Brandl, T. Reinecke and M. Muhler, *Electrochim. Acta*, 2009, **54**, 4208-4215.

40. M. Liu and J. Li, *Electrochim. Acta*, 2015, **154**, 177-183.

41. R. Sharma and K. K. Kar, *Mater. Lett.*, 2014, **137**, 150-152.

42. H. Hu, B. Zhao, M. E. Itkis and R. C. Haddon, *J. Phys. Chem. B*, 2003, **107**, 13838-13842.

43. R. Sharma and K. K. Kar, *Electrochim. Acta*, 2015, **156**, 199-206.

44. R. Sharma and K. K. Kar, *J. Mater. Chem. A*, 2015, **3**, 11948-11959.

45. M. Saravanan, P. Sennu, M. Ganesan and S. Ambalavanan, *J. Electrochem. Soc.*, 2013, **160**, A70-A76.

46. B. Seger and P. V. Kamat, *J. Phys. Chem. C*, 2009, **113**, 7990-7995.

47. S. Trasatti and O. Petrii, *Pure Appl. Chem.*, 1991, **63**, 711-734.

48. D. Geng, Y. Chen, Y. Chen, Y. Li, R. Li, X. Sun, S. Ye and S. Knights, *Energy Environ. Sci.*, 2011, **4**, 760-764.

49. C. Wang, H. Daimon, T. Onodera, T. Koda and S. Sun, *Angew. Chem. Int. Ed.*, 2008, **47**, 3588-3591.

50. H. A. Gasteiger, J. E. Panels and S. G. Yan, *J. Power Sources*, 2004, **127**, 162-171.

51. N. M. Markovic, H. A. Gasteiger and P. N. Ross, *J. Phys. Chem.*, 1996, **100**, 6715-6721.

52. W.-J. Jiang, J.-S. Hu, X. Zhang, Y. Jiang, B.-B. Yu, Z.-D. Wei and L.-J. Wan, *J. Mater. Chem. A*, 2014, **2**, 10154-10160.

53. J. Wu, J. Zhang, Z. Peng, S. Yang, F. T. Wagner and H. Yang, *J. Am. Chem. Soc.*, 2010, **132**, 4984-4985.

54. J. Yuan, B. He, L. Hong, J. Lu, J. Miao and L. Niu, *J. Mater. Chem.*, 2012, **22**, 19658-19665.

55. S. Zhang, Y. Shao, G. Yin and Y. Lin, *J. Mater. Chem.*, 2010, **20**, 2826-2830.

56. W. Zhu, D. Ku, J. P. Zheng, Z. Liang, B. Wang, C. Zhang, S. Walsh, G. Au and E. J. Plichta, *Electrochim. Acta*, 2010, **55**, 2555-2560.

57. R. Borup, J. Meyers, B. Pivovar, Y. S. Kim, R. Mukundan, N. Garland, D. Myers, M. Wilson, F. Garzon and D. Wood, *Chem. Rev. (Washington, DC, U. S.)*, 2007, **107**, 3904-3951.

Graphical and textual abstract

Hierarchically structured fuel cell cathode catalysts consisting of Pt-nanoparticle clusters coated on a CNT-based, ORR active catalyst support were synthesized.